Article

Excitation-dependent perovskite/polymer films for ultraviolet visualization

Junlu Sun [a,b,1], Tianshu Li [c,1], Lin Dong [b,*], Qilin Hua [a], Shuai Chang [d], Haizheng Zhong [d], Lijun Zhang [c,*], Chongxin Shan [b,*], Caofeng Pan [a,*]

[a] CAS Center for Excellence in Nanoscience, Beijing Key Laboratory of Micro-nano Energy and Sensor, Beijing Institute of Nanoenergy and Nanosystems, Chinese Academy of Sciences, Beijing 100083, China
[b] Henan Key Laboratory of Diamond Optoelectronic Materials and Devices Key Laboratory of Materials Physics (Ministry of Education), School of Physics and Microelectronics, Zhengzhou University Zhengzhou 450001, China
[c] State Key Laboratory of Integrated Optoelectronics, Key Laboratory of Automobile Materials (Ministry of Education), School of Materials Science and Engineering, Jilin University, Changchun 130012, China
[d] MIIT Key Laboratory for Low-Dimensional Quantum Structure and Devices, School of Materials Science & Engineering, Beijing Institute of Technology, Beijing 100081, China

A R T I C L E   I N F O

A B S T R A C T

Ultraviolet (UV) visualization has extensive applications in military and civil fields such as security monitoring, space communication, and wearable equipment for health monitoring in the internet of things (IoT). Due to their remarkable optoelectronic features, perovskite materials are regarded as promising candidates for UV light detecting and imaging. Herein, we report for the first time the excitation-dependent perovskite/polymer films with dynamically tunable fluorescence ranging from green to magenta by changing the UV excitation from 260 to 380 nm. And they still render dynamic multi-color UV light imaging with different polymer matrixes, halogen ratios, and cations of perovskite materials. The mechanism of its fluorescence change is related to the chloride vacancies in perovskite materials. A patterned multi-color ultraviolet visualization pad is also demonstrated for visible conversion of the UV region. This technique may provide a universal strategy for information securities, UV visualizations, and dynamic multi-color displays in the IoT.

© 2022 Science China Press. Published by Elsevier B.V. and Science China Press. All rights reserved.

1. Introduction

Imaging in the ultraviolet (UV) light range (or called ultraviolet visualization) has significant applications in flame monitoring [1–5], optical communication [6–9], and missile-plume detection while the interference in the visible range needs to be suppressed. The UV light could be divided into three parts: UVA (400–315 nm), UVB (315–280 nm), and UVC (280–190 nm). Since UVC light cannot go through the atmosphere, it is beneficial for precise detection of flame monitoring and missile-plume. As the most common material for commercial UV light imaging, silicon exhibits its intrinsic limitations including poor selectivity against visible and infrared photons [10], lower quantum efficiency for UV light [11], and degradation under UV irradiation [12]. Therefore, it is highly demanded to use alternative down-conversion and excitation-dependent materials (such as organic quantum dots [13,14], inorganic quantum dots [15,16], and rare-earth compounds [17,18]) to realize UV light imaging with higher efficiency.

Perovskite materials have been utilized in solar cells [19–23], light-emitting diodes (LEDs) [24–28], photodetectors (PDs) [29–32], fluorescence films [33–36], and lasers [37–42] due to remarkable optoelectronic features such as large optical absorption coefficient and high quantum yield. They are also appropriate fluorescent materials for UV light visualization and precisely tuned emission wavelength could be achieved simply by changing the halogen constitution or element doping [25–27,33–37]. Perovskite multi-color displays have been demonstrated by assembling such fluorescent films with different color-rendering. However, their colors could not reflect the real-time variation of incident UV light within an individual device, which limits their applications in UV light imaging.

Here, we present excitation-dependent perovskite/polymer films with dynamically tunable multi-color from green to magenta under UV excitation ranging from 260 to 380 nm. The influence of

---

the cation type and the chemical composition of excitation-dependent perovskite/polymer films on their photoluminescence (PL) spectra are investigated. In different polymer matrixes and cations of perovskite materials, the films still render dynamic multi-color UV light imaging. Spectroscopy analysis and theoretical calculation indicate that the multi-color rendering property is related to the Cl vacancy in perovskite materials. Finally, a mapping table of UV wavelength versus visible color is obtained based on excitation-dependent perovskite/polymer patterns, which visually identify specific wavelengths in the UV region. The one-to-one mapping of UV visualization perovskite/polymer films reported here could realize dynamical display within an individual device, which is distinguished from other perovskite/polymer films [40–43]. And the excitation-dependent perovskite/polymer film, as information carriers, may offer a powerful platform for dynamic anti-counterfeiting in information securities, pattern recognition in optical communication, and multi-color fluorescent tags in internet of things (IoT).

2. Experimental

2.1. Materials

Lead chloride ($PbCl_2$, 99.9%), lead (II) bromide ($PbBr_2$, 99.9%), methylammonium chloride (MACl, 99.9%), ethylamine chloride (EACl, 99.9%), propylamine chloride (PACl, 99.9%), butylamine chloride, (BACl, 99.9%), and cesium chloride (CsCl, 99.9%) were obtained from Xi'an Polymer Light Technology Co. (China). *N,N*-dimethylformamide (DMF, 99.9%), dimethyl sulfoxide (DMSO, 99.5%), and poly(vinylidene fluoride) (PVDF, M_w 400,000), polymethyl methacrylate (PMMA), polyacrylonitrile (PAN) were purchased from Sigma-Aldrich (USA).

2.2. Fabrication of excitation-dependent perovskite/polymer films and pattern

PbX_2 and MAX (X: Cl, Br; 1 mmol) were dissolved in the DMF/DMSO (1 mL) to obtain perovskite solution A. The polymer (PVDF, or PAN, or PMMA) of 0.8 g was dissolved in DMF (5 mL) to obtain polymer solution B. Then, perovskite solution A was added into polymer solution B to obtain the precursor solution with various weight ratios. The precursor solution was spin-coated on a glass substrate at 2000 r/min and then transferred into a vacuum oven to rapidly remove the DMF at low pressure (0.01 MPa) for 5 min. Finally, $EAPbCl_3$/PVDF film, $PAPbCl_3$/PVDF film, and $BAPbCl_3$/PVDF film were fabricated by substituting MACl with EACl, PACl, and BACl. As for the multi-color perovskite/polymer pattern, the screen printing was utilized to obtain the office logo "BINN" and "ZZU".

2.3. Characterization and measurements

The X-ray diffraction (XRD) and Fourier transform infrared (FTIR) spectra of perovskite/polymer film were obtained by X-ray diffraction (X'Pert3 Powder) θ–2θ scan with Cu Kα radiation and Nicolet 6700 spectrometer (Thermo Fisher Scientific, USA). The optical properties of perovskite/polymer film were obtained by UV–visible spectra (UV-3600 Shimadzu, Japan) and photoluminescence spectrometer (FLS1000, Edinburgh, UK).

2.4. Theoretical method

First-principles calculations were performed within the framework of density-functional theory, as implemented in the Vienna *Ab initio* Simulation Package. The interaction between core and valence electrons was explained using the frozen-core projector

augmented wave pseudopotentials. The exchange–correlation functional was based on Perdew-Burke-Ernzerhof functional for geometry optimization, electronic structures and defect formation energies. In our calculations for primitive cells, the kinetic energy cutoff for plane-wave basis was set to be 400 eV in conjunction with k-mesh grid $5 \times 5 \times 5$ for Brillouin zone sampling. For the supercell calculations, a $2 \times 2 \times 2$ supercell based on 12-atom unit cell and a Monkhost k-mesh grid $3 \times 3 \times 3$ were used.

The formation energies (E^f) are calculated according to the equation:

$$E^f(D^q) = \left(E_D^q - E_h\right) - \sum_i n_i\left(\mu_i + \mu_i^{bulk}\right) + q(\varepsilon_{VBM} + \varepsilon_f) + \Delta E_{corr}, \quad (1)$$

where E_D^q is the total energy of the defect at the charge state q in the supercell, E_h is the energy of the defect-free supercell and n_i is the difference in the number of atoms for the ith atomic species between the defect-containing and defect-free supercells. μ_i is the chemical potential of the ith atomic species relative to its bulk chemical potential μ_i^{bulk}. ε_{VBM} is the energy of valence-band maximum (VBM) of the defect-free material and ε_f is the Fermi energy referenced to ε_{VBM}.

Because of the large difference in lattice relaxations around V_{Cl}^0 and V_{Cl}^-, the $\varepsilon(0/-1)$ transition level should be significantly different from the optical transition level. During the optical transition process, the time scale is much shorter than structural relaxation, maintaining the unchanged initial state of atomic configuration. We investigate the absorption and emission processes by calculating configuration coordinate diagram. With the V_{Cl}^- acting as an initial state, an electron is excited to the CBM after absorbing the energy of a photon, resulting in a neutral charged state of Cl vacancy (V_{Cl}). The calculated absorption energy for the vertical transition is 2.97 eV. For the emission process, an electron transfer to V_{Cl}^0 from the conduction band, leading to V_{Cl}^-, peaks at 2.23 eV. The predicted configuration coordinate diagram indicates that the green luminescence is caused by V_{Cl}.

The thermodynamic transition energy between two charge states q and $q\prime$ can be determined by

$$\varepsilon(q/q') = \left[E^f(D, q'; \varepsilon_f = 0) - E^f(D, q; \varepsilon_f = 0)\right]/(q - q'). \quad (2)$$

When the Fermi level is below this energy, the charge state q is stable; otherwise, the charge state $q\prime$ is stable.

3. Results and discussion

Fig. 1a illustrates the perovskite ($CH_3NH_3PbCl_3$, $MAPbCl_3$) capable of rendering different colors (green to purple) as the excitation wavelength changes. To improve the stability of perovskite, the perovskite nanocrystals are embedded in polymers. The perovskite/polymer composite film is obtained by spin-coating the solution of $MAPbCl_3$ and PVDF in DMF/DMSO. The detailed fabrication process is described in the Experimental section. The XRD patterns of $MAPbCl_3$/PVDF and PVDF are shown in Fig. 1b. The peaks at 15.1°, 30.3°, and 33.8° are attributed to the scattering from the (100), (200), and (210) lattice surface of the perovskite $MAPbCl_3$ [29], while the broad peak at 20.7° is due to the overlap of (110) and (200) crystal face of β-phase PVDF [33]. FTIR spectroscopy is also utilized to characterize the multi-color $MAPbCl_3$/PVDF film, as shown in Fig. 1c. The characteristic peaks at 510 and 839 cm^{-1} are attributed to the absorption band of β-phase PVDF [33,34,43]. The film exhibits high optical transparency (>80%) over the entire visible region range, as evidenced in Fig. 1d, where the corresponding photo of a multi-color $MAPbCl_3$/PVDF film is also shown as an inset. The pattern of the official logo "BINN" could be clearly recognized through the film.
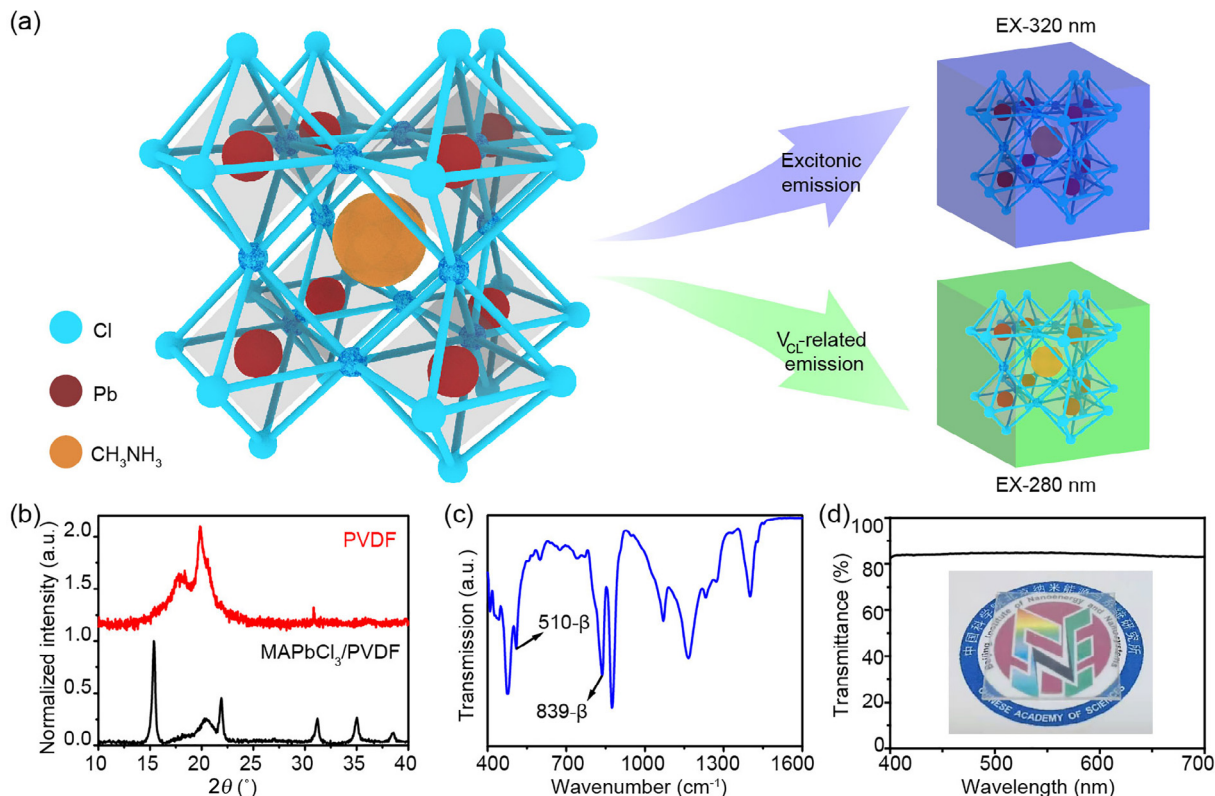
Fig. 1. (Color online) Illustration and characterizations of multi-color perovskite/polymer film. (a) Crystalline structure of multi-color perovskite (EX: excitation, EM: emission, V_{Cl}: Cl vacancy). (b–d) XRD, FTIR, and optical transmittance spectra of $MAPbCl_3$/PVDF film; inset: the photo of $MAPbCl_3$/PVDF film.

The color rendering evolution of $MAPbCl_3$/PVDF film under changing excitation-wavelength is investigated by PL spectra, as shown in Fig. 2a. Three emission centers at 397, 520, and 713 nm are observed, which can be attributed to the emissions from excitonic emission of $MAPbCl_3$, V_{Cl}-related emission in $MAPbCl_3$, and the substrate, respectively. The highest hot point is found at around (EX = 275 nm, EM = 520 nm; EX: excitation, EM: emission). The PL excitation spectra acquired at the wavelength of these emission centers are illustrated in Fig. 2b. The PL intensities of three emission centers under various excitation wavelengths are quite different, resulting in the overall changed fluorescence color. The perovskite/polymer film displays green color under excitation of 260–300 nm; while turning blue under 320–360 nm excitation, and magenta with excitation of 380 nm. The relative change in the emission intensities of 397, 520, and 713 nm led to the dynamic multi-color display. Corresponding photos of $MAPbCl_3$/PVDF film under various excitation wavelengths are obtained and presented in Fig. 2d, in which various colors are rendered as a combination of the blue, green, and magenta emissions. The Commission International de l'Eclairage (CIE) coordinate diagram demonstrated in Fig. 2c is based on the PL spectra of $MAPbCl_3$/PVDF film under different excitation wavelengths. The tunable color rendering characteristics of perovskite/polymer film are clearly demonstrated. The multi-color $MAPbCl_3$/PVDF film with the best PL quantum yield of 4.68% under excitation wavelength 270 nm is presented in Fig. S1a, b (online). The corresponding PL lifetime decay of the emission center at 520 nm is 1.31 μs (Fig. S1c, d online) [15,17]. And the film renders excellent long-term stability as shown in Fig. S2 (online). The $MAPbCl_3$/PVDF film still reveals over 90% PL intensity after 12 h continuous irradiation and measurement.

To optimize the multi-color display performance of perovskite/polymer, influence factors such as substrate, polymer species, halogens, and cations of perovskite materials are studied. Firstly, Fig. 3a shows the PL spectra of the substrate under excitation wavelength 380 nm, which is consistent with the emission center (713 nm) of perovskite/polymer film on the substrate. The corresponding PL excitation spectra, CIE chromaticity diagram, and the photo of glass substrate under excitation wavelength 380 nm are consistent with those of multi-color $MAPbCl_3$/PVDF film on the substrate (Fig. S3 online). That is to say, the emission center at 713 nm is attributed to the substrate. Then, the polymer PVDF film is investigated and shown in Fig. S4 (online). The PVDF film exhibits similar transparency, compared with the obvious green color of the $MAPbCl_3$/PVDF film under UV excitation 302 and 365 nm. The PL excitation-emission spectra mapping of PVDF film in Fig. S4c (online) also confirms the similar transparency without obvious luminescence centers. The multi-color characteristic of perovskite/polymer films with PMMA or PAN are also presented in Fig. 3b and Fig. S5 (online). They all present identical luminescence centers, and demonstrate green, blue, and magenta color under UV excitation 280, 320, and 380 nm, respectively. Therefore, the multi-color display property of perovskite/polymer would not affect by the polymer matrix.

As for the perovskite $MAPbCl_3$ of perovskite/polymer films, the halogen chloride and MA could be substituted by other halogens and cations separately. The cation substitution of MA by ethylamine (EA), propylamine (PA), butylamine (BA), and cesium (Cs) is first investigated. All products present multi-color features with three luminescence centers under various UV excitations, as shown in Fig. 3c and Fig. S6 (online). The inorganic cation cesium (Cs) is also used to explore the multi-color characteristic of $CsPbCl_3$/PVDF
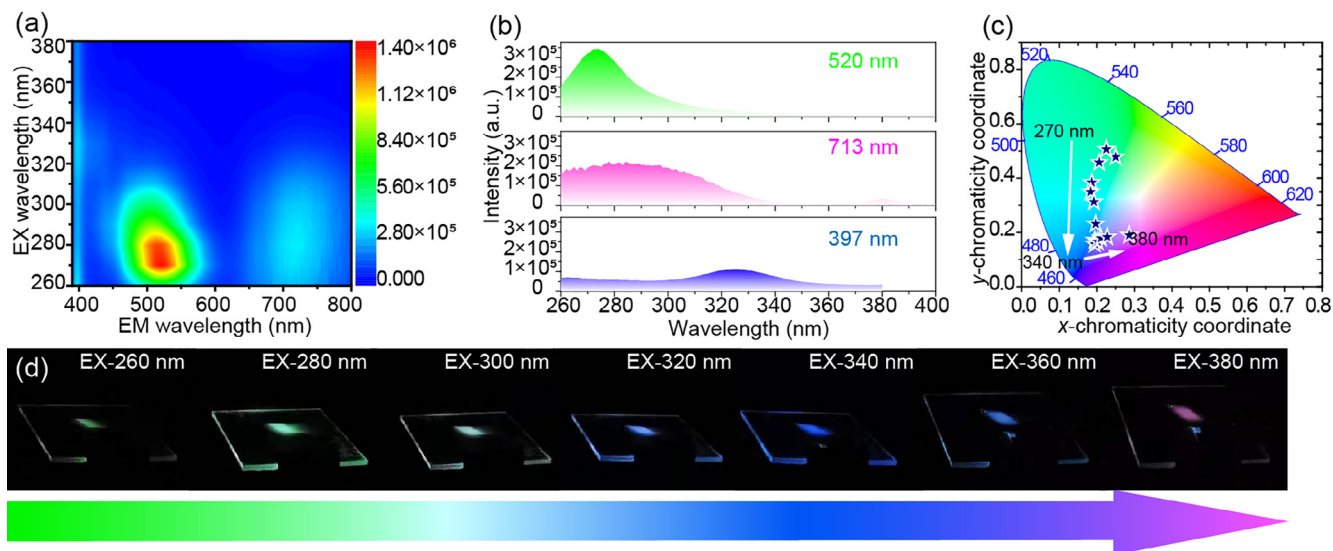
Fig. 2. (Color online) Excitation-dependent PL and color rendering of the MAPbCl₃/PVDF film. (a) PL excitation-emission spectra. (b) PL excitation spectra acquired at 397, 520, and 713 nm. (c) CIE chromaticity diagram. (d) Photos of MAPbCl₃/PVDF film on a glass substrate under various excitation wavelengths.
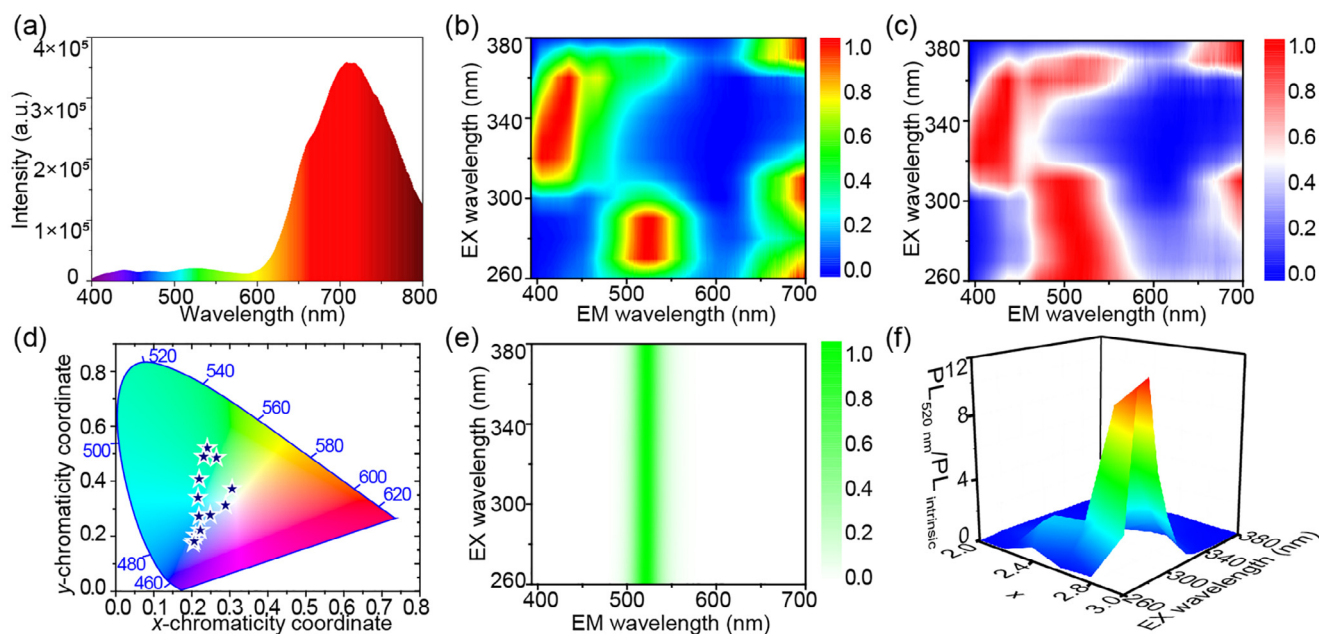

Fig. 3. (Color online) Influence parameters of multi-color MAPbCl₃/PVDF film on substrate. (a) PL spectra of the substrate. Normalized PL excitation-emission spectra mapping of (b) MAPbCl₃/PAN and (c) EAPbCl₃/PVDF film. (d) CIE chromaticity diagram of CsPbCl₃/PVDF film. (e) Normalized PL excitation-emission spectra mapping of MAPbBr₃/PVDF film. (f) The relationship between the PL intensity of V_{Cl}-related emission and the excitonic emission intensity of MAPbCl$_x$Br$_{3-x}$/PVDF film (x = 2.0, 2.2, 2.4, 2.6, 2.8, and 3.0).

film. As shown in Fig. 3d and Fig. S7 (online), two luminescence centers (418 and 520 nm), variational colors in CIE chromaticity diagram, and multi-color photos of CsPbCl₃/PVDF film are obtained. Hence, changing the cation will not impair the multi-color characteristic of the perovskite/polymer films.

To gain a deeper insight into the multi-color characteristics, a series of MAPbCl$_x$Br$_{3-x}$/PVDF (x = 0, 2.0, 2.2, 2.4, 2.6, 2.8, and 3.0) films are prepared and investigated. The normalized PL excitation-emission spectra mapping of MAPbBr₃/PVDF film depicts only one luminescence center at 518 nm on UV excitation from 260 to 380 nm (Fig. 3e), i.e., the MAPbBr₃/PVDF film shows no multi-color characteristics. Usually, the excitonic emission of MAPbBr₃/PVDF composites exhibits high PL quantum yield of

90% [33,43], whereas the emissions related to the substrate and bromine vacancy (V_{Br}) are rather weaker. Therefore, the defect-induced emission and substrate luminescence are fully suppressed. Then, perovskite materials (MAPbCl$_x$Br$_{3-x}$) with different halogens ratio is studied. The halogen species have a great influence on the multi-color characteristics of perovskite/polymer film. The corresponding PL excitation and emission spectra of MAPbCl$_x$Br$_{3-x}$/PVDF films are collected (Figs. S8, S9 online). They all present the multi-color characteristics with three luminescence centers mentioned above (excitonic emission, V_{Cl}-related emission in perovskite materials, and the substrate) under UV excitation from 260 to 380 nm. The intensity of the PL emission related to Cl vacancy decrease gradually as the ratio of chloride reduces, which is clearly
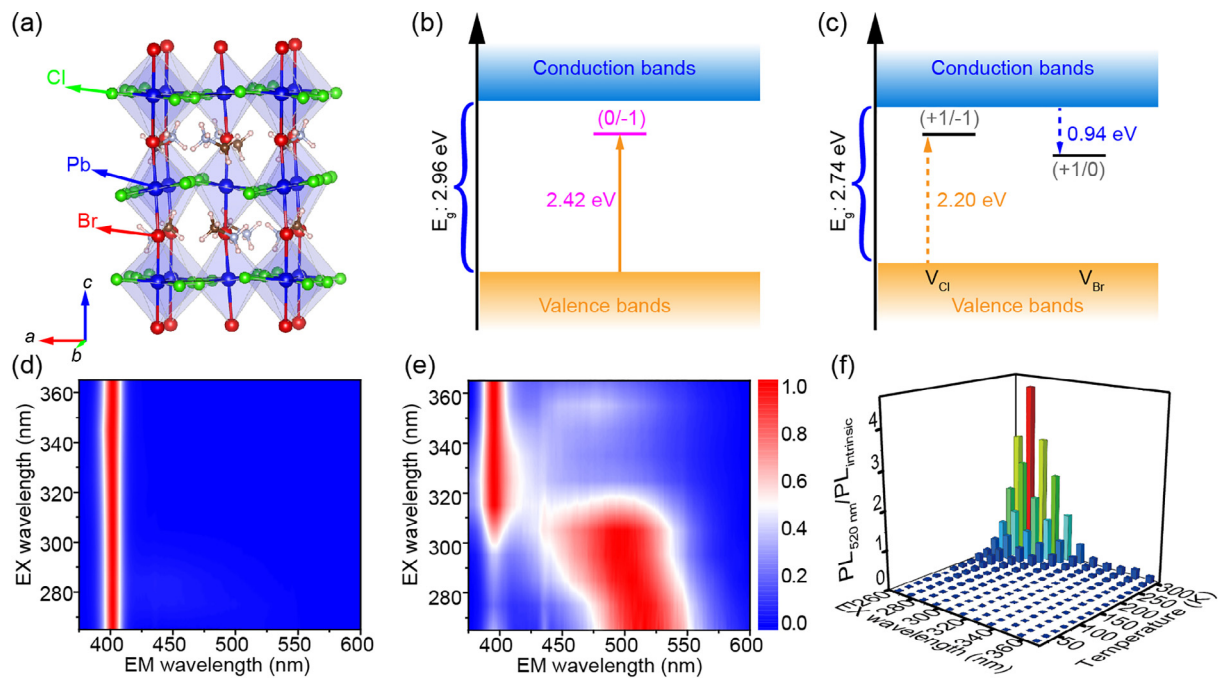
Fig. 4. (Color online) Theoretical simulation and experimental verification of V_{Cl} related emissions. (a) Crystal structure of MAPbCl$_x$Br$_{3-x}$. (b, c) Transition levels of MAPbCl$_3$ and MAPbCl$_2$Br. (d, e) PL excitation-emission spectra mapping of MAPbCl$_3$/PVDF film acquired at 20 and 300 K. (f) The relationship between the PL intensity of chloride vacancy at 520 nm and the excitonic emission of MAPbCl$_3$ on UV excitation from 265 to 365 nm at various temperatures (20–300 K).

shown in PL excitation spectra of MAPbCl$_x$Br$_{3-x}$/PVDF films (Fig. S10 online). The colors of perovskite/polymer films with various halogen ratios under excitation wavelength 275 nm change from green to blue gradually as the ratio of chloride reduce (Figs. S8, S9 online). Fig. 3f depicts the PL intensity relationship between the Cl vacancy-related emission at 520 nm and the excitonic emission of MAPbCl$_x$Br$_{3-x}$/PVDF film with variant x. When the value of x is higher than 2.8, an abrupt increase in the PL$_{520\ nm}$: PL$_{402\ nm}$ is observed, the optimized ratio (x value) of excitation-dependent perovskite/polymer (MAPbCl$_x$Br$_{3-x}$/PVDF) film is 3.0. Therefore, tuning the composition of halogen species is very important for the multi-color display of the perovskite/polymer film.

Theoretical calculation is carried out to verify the mechanism of the multi-color characteristic of MAPbCl$_3$/PVDF film. Fig. 4a depicts the crystal structure of mixed halogen perovskite MAPbCl$_x$Br$_{3-x}$ of cubic symmetry. The *ab initio* calculation indicates that V_{Cl} can introduce an acceptor transition level (0/−1) at 2.42 eV above the valence band maximum (VBM) of MAPbCl$_3$, as shown in Fig. 4b and Figs. S11, S12 (online), in accordance with the previous theoretical works [44–51]. For a defect-containing system, the defect transition level indicates the energy it takes to alter its charge states. Thus, the charge state of V_{Cl} can be altered between $q = 0$ and $q = −1$ with the transition energy higher than 2.42 eV. Therefore, this mid-gap defect energy level caused by V_{Cl} provides an intermediary allowing carrier transfer between the defect level (0/–1) and VBM, which contributes to the observed PL luminescence center at 520 nm.

As for MAPbCl$_2$Br, V_{Cl} and V_{Br} act as deep-level defects. There is only one transition level (+1/−1) for V_{Cl} within the gap of MAPbCl$_2$-Br. Theoretical results indicate the V_{Cl} is a dipolar defect in MAPbCl$_2$Br, which is similar to the situation in MAPbCl$_3$. The transition level ε(+1/−1) of V_{Cl} is 2.20 eV above the VBM. Whereas, V_{Br} acts as a deep-level donor with the transition level ε(+1/0) of 0.94 eV below the CBM of MAPbCl$_2$Br, as shown in Fig. 4c. The stable regions under different Br chemical potentials are shown in Fig. S13 (online). The Cl-rich chemical condition (A and B points)

and Cl-poor & Br-poor condition (C point) were selected to calculate the formation energies (E^f). Under Cl-rich condition, the E^f of V_{Br} is lower than that of V_{Cl}, indicating that the formation of V_{Cl} will be suppressed by halogen Br. So, the luminescence center at 520 nm gradually disappears as the ratio of halogen bromine increases.

To further explore the relationship between the V_{Cl} and multi-color characteristics, PL spectra of MAPbCl$_3$/PVDF film under UV excitation ranging from 265 to 365 nm are obtained at temperatures from 20 to 300 K (Figs. S14, S15 online). It exhibits dual-dependent features, i.e., excitation-dependent and temperature-dependent. The excitation-dependent characteristic renders throughout the entire temperature range surveyed in this work (20–300 K). As for the temperature-dependent characteristic, only one excitonic emission of MAPbCl$_3$ at 20 K (Fig. 4d) exists and the PL related to defect-induced emission (at 520 nm) gradually arises continuously with the temperature increasing (Fig. 4e), and reaches its zenith at 300 K under the UV excitation of 275 nm (Fig. 4f), i.e., the best temperature of excitation-dependent characteristic is room temperature. Therefore, the multi-color display characteristic of perovskite/polymer film on UV excitation is closely correlated with the defect-induced emission (chloride vacancy) of the perovskite, which inspires a novel approach to UV visualization. The excitation wavelengths of the luminescence center based on chlorine vacancies are near 275 nm, which may be related to PbCl$_2$. As shown in Fig. S16a (online), absorption spectra of MAPbCl$_3$/PVDF film render two absorption peaks at 275 and 397 nm. The former absorption stems from MAPbCl$_3$, while the latter is attributed to the absorption of PbCl$_2$, in well with the absorption spectra of PbCl$_2$/PVDF films. The residual PbCl$_2$ is also evidenced in the XRD patterns collected by the MAPbCl$_3$/PVDF film (Fig. S16b, c online).

Based on the multi-color characteristics of perovskite/polymer film, the detection and visual imaging of a specific wavelength in the UV region are demonstrated. Different patterns of the official logo "BINN" and "ZZU" are prepared via screen-printing by using MAPbCl$_3$/PVDF solution as ink (Fig. S17 online). The color of the
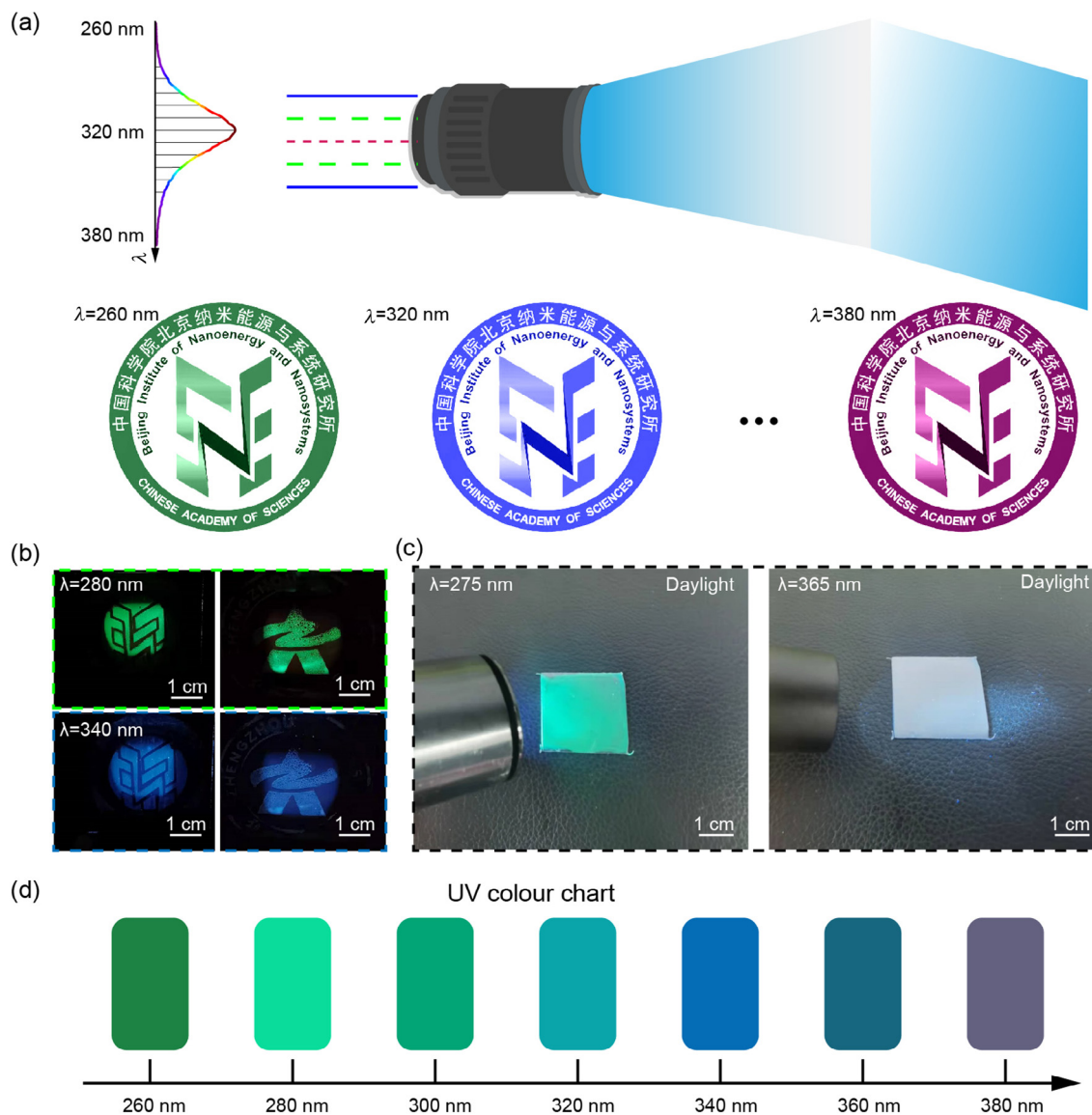
Fig. 5. (Color online) Demonstration of multi-color perovskite/polymer pattern film and visualization of ultraviolet light. (a) Schematic of the experimental set-up for multi-color display by varying the excitation wavelength from 260 to 380 nm. (b) Photographs of the perovskite/polymer film patterned with the official logo of "BINN" and "ZZU" under UV excitation of 280 and 340 nm. (c) Photographs of multi-color perovskite/polymer film with UV excitation of 275 and 365 nm under daylight circumstance. (d) UV color chart demonstrating the feasibility of using perovskite/polymer film to visually distinguish specific wavelengths in the UV region.

patterned luminescence image varies from green to magenta as the UV excitations change from 260 to 380 nm (Fig. 5a). As shown in Fig. 5b, green and blue images of these patterns are captured under the UV excitation of 280 and 340 nm, respectively. Other colored patterns under excitation wavelengths of 260, 300, 320, 360, and 380 nm are collected in Fig. S17 (online). Moreover, the multi-color perovskite/polymer film can also present the green color with the excitation of a 275 nm UV lamp under daylight circumstances. But the color of perovskite/polymer film is unchanged with the excitation of UV 365 nm (Fig. 5c and Video S1 online). Therefore, this film can be utilized under daylight circumstances. Hence, a UV color chart is obtained (Fig. 5d), which could be utilized to visually identify the specific wavelength in the UV region. And the multi-color perovskite/polymer films can be used as information carriers based on the UV color chart for dynamic anti-counterfeiting in information securities, pattern recognition in optical communication, and multi-color fluorescent tags in IoT.

4. Conclusion

Perovskite/polymer films with multi-color fluorescence under different UV irradiation are obtained through spin-coating. The colors of these films could be dynamically tuned from green to magenta when changing the UV excitation wavelength from 260 to 380 nm. Parameters including substrate, polymer species, cations, halogen species, and halogen ratios of perovskite are explored to study the mechanism of multi-color characteristics of perovskite/polymer films, as well as theoretical calculations. The multi-color display of perovskite/polymer films is a result of the competing processes related to V_{Cl}-related emission and excitonic emission of perovskite materials. Perovskite/polymer patterns are fabricated by screen-print to demonstrate the detection and imaging the specific UV light wavelengths. The multi-color perovskite/polymer film may offer a novel approach to multi-color display, UV visualization and other potential applications in IoT.

Conflict of interest

Acknowledgments

Author contributions

Junlu Sun, Lin Dong, Chongxin Shan, and Caofeng Pan conceived the project and designed the experiments. Junlu Sun carried out most of the experiments and analyzed the data. Tianshu Li and Lijun Zhang contributed to the theoretical calculations. Shuai Chang, Qilin Hua, and Haizheng Zhong analyzed the data. All the authors discussed the results and commented on the paper.

Appendix A. Supplementary materials

Supplementary materials to this article can be found online at https://doi.org/10.1016/j.scib.2022.08.009.

References

[1] Lin C-N, Lu Y-J, Yang X, et al. Diamond-based all-carbon photodetectors for solar-blind imaging. Adv Opt Mater 2018;6:1800068.

[2] Adinolfi V, Ouellette O, Saidaminov MI, et al. Fast and sensitive solution-processed visible-blind perovskite UV photodetectors. Adv Mater 2016;28:7264–8.

[3] Sun JQ, Cheng X, Ding MD, et al. Extreme ultraviolet imaging of three-dimensional magnetic reconnection in a solar eruption. Nat Commun 2015;6:7598.

[4] Peng Y, Lu J, Peng D, et al. Dynamically modulated GaN whispering gallery lasing mode for strain sensor. Adv Funct Mater 2019;29:1905051.

[5] Dong L, Niu S, Pan C, et al. Piezo-phototronic effect of CdSe nanowires. Adv Mater 2012;24:5470–5.

[6] Sang L, Liao M, Sumiya M. A comprehensive review of semiconductor ultraviolet photodetectors: From thin film to one-dimensional nanostructures. Sensors 2013;13:10482–518.

[7] Chen B, Wan Y, Xie Z, et al. Low dark current high gain InAs quantum dot avalanche photodiodes monolithically grown on Si. ACS Photonics 2020;7:528–33.

[8] Liang Y-C, Liu K-K, Wu X-Y, et al. Lifetime-engineered carbon nanodots for time division duplexing. Adv Sci 2021;8:2003433.

[9] Shen C-L, Lou Q, Lv C-F, et al. Bright and multicolor chemiluminescent carbon nanodots for advanced information encryption. Adv Sci 2019;6:1802331.

[10] Xing J, Zhao K, Lu HB, et al. Visible-blind, ultraviolet-sensitive photodetector based on $SrTiO_3$ single crystal. Opt Lett 2007;32:2526–8.

[11] Zou J, Zhang Q, Huang K, et al. Ultraviolet photodetectors based on anodic TiO_2 nanotube arrays. J Phys Chem C 2010;114:10725–9.

[12] Nasiri N, Jin D, Tricoli A. Nanoarchitechtonics of visible-blind ultraviolet photodetector materials: critical features and nano-microfabrication. Adv Opt Mater 2019;7:1800580.

[13] Liang Y-C, Shang Y, Liu K-K, et al. Water-induced ultralong room temperature phosphorescence by constructing hydrogen-bonded networks. Nano Res 2020;13:875–81.

[14] Gu L, Wu H, Ma H, et al. Color-tunable ultralong organic room temperature phosphorescence from a multicomponent copolymer. Nat Commun 2020;11:944.

[15] Li F, Wang X, Xia Z, et al. Photoluminescence tuning in stretchable PDMS film grafted doped core/multishell quantum dots for anticounterfeiting. Adv Funct Mater 2017;27:1700051.

[16] Liu Y, Han F, Li F, et al. Inkjet-printed unclonable quantum dot fluorescent anti-counterfeiting labels with artificial intelligence authentication. Nat Commun 2019;10:2409.

[17] Ding M, Dong B, Lu Y, et al. Energy manipulation in lanthanide-doped core-shell nanoparticles for tunable dual-mode luminescence toward advanced anti-counterfeiting. Adv Mater 2020:2002121.

[18] Yao W, Tian Q, Wu W. Tunable emissions of upconversion fluorescence for security applications. Adv Opt Mater 2019;7:1801171.

[19] Sun J, Hua Q, Zhou R, et al. Piezo-phototronic effect enhanced efficient flexible perovskite solar cells. ACS Nano 2019;13:4507–13.

[20] Lei Y, Chen Y, Zhang R, et al. A fabrication process for flexible single-crystal perovskite devices. Nature 2020;583:790–5.

[21] Li N, Niu X, Li L, et al. Liquid medium annealing for fabricating durable perovskite solar cells with improved reproducibility. Science 2021;373:561.

[22] Sun J, Li N, Dong L, et al. Interfacial-engineering enhanced performance and stability of zno nanowire-based perovskite solar cells. Nanotechnology 2021;32:475204.

[23] Peng D, Liu X, Pan C. Epitaxial lift-off for controllable single-crystalline perovskites. Sci Bull 2021;66:6–8.

[24] Wang C, Han D, Wang J, et al. Dimension control of *in situ* fabricated $CsPbClBr_2$ nanocrystal films toward efficient blue light-emitting diodes. Nat Commun 2020;11:6428.

[25] Song J, Li J, Li X, et al. Quantum dot light-emitting diodes based on inorganic perovskite cesium lead halides ($CsPbX_3$). Adv Mater 2015;27:7162–7.

[26] Fang T, Wang T, Li X, et al. Perovskite QLED with an external quantum efficiency of over 21% by modulating electronic transport. Sci Bull 2021;66:36–43.

[27] Song H, Liu X, Wang B, et al. High production-yield solid-state carbon dots with tunable photoluminescence for white/multi-color light-emitting diodes. Sci Bull 2019;64:1788–94.

[28] Ma Z, Shi Z, Yang D, et al. High color-rendering index and stable white light-emitting diodes by assembling two broadband emissive self-trapped excitons. Adv Mater 2021;33:2001367.

[29] Cheng Z, Liu K, Yang J, et al. High-performance planar-type ultraviolet photodetector based on high-quality $CH_3CH_3PbCl_3$ perovskite single crystals. ACS Appl Mater Interfaces 2019;11:34144–50.

[30] Wu W, Han X, Li J, et al. Ultrathin and conformable lead halide perovskite photodetector arrays for potential application in retina-like vision sensing. Adv Mater 2021;33:2006006.

[31] Wu W, Wang X, Han X, et al. Flexible photodetector arrays based on patterned $CH_3CH_3PbI_{3-x}Cl_x$ perovskite film for real-time photosensing and imaging. Adv Mater 2019;31:1805913.

[32] Yang Z, Xu Q, Wang X, et al. Large and ultrastable all-inorganic $CsPbBr_3$ monocrystalline films: low-temperature growth and application for high-performance photodetectors. Adv Mater 2018;30:1802110.

[33] Zhou Q, Bai Z, Lu W, et al. *In situ* fabrication of halide perovskite nanocrystal-embedded polymer composite films with enhanced photoluminescence for display backlights. Adv Mater 2016;28:9163–8.

[34] Imran M, Mai BT, Goldoni L, et al. Switchable anion exchange in polymer-encapsulated $APbX_3$ nanocrystals delivers stable all-perovskite white emitters. ACS Energy Lett 2021;6:2844–53.

[35] Zhang R, Xu X, Mao X, et al. Excitation-dependent emission in all-inorganic lead-free $Cs_2ScCl_5 \cdot H_2O$ perovskite crystals. Laser Photonics Rev 2022;16:2100689.

[36] Wei J-H, Liao J-F, Zhou L, et al. Indium-antimony-halide single crystals for high-efficiency white-light emission and anti-counterfeiting. Sci Adv 2021;7:eabg3989.

[37] Peng H, Tian Y, Yu Z, et al. $(C_{16}H_{28}N)_2SbCl_5$: a new lead-free zero-dimensional metal-halide hybrid with bright orange emission. Sci China Mater 2022;65:1594–600.

[38] Dai G, Wang L, Cheng S, et al. Perovskite quantum dots based optical fabry–pérot pressure sensor. ACS Photonics 2020;7:2390–4.

[39] Li M, Gao Q, Liu P, et al. Amplified spontaneous emission based on 2D ruddlesden–popper perovskites. Adv Funct Mater 2018;28:1707006.

[40] Yang Z, Lu J, Zhuge M, et al. Controllable growth of aligned monocrystalline $CsPbBr_3$ microwire arrays for piezoelectric-induced dynamic modulation of single-mode lasing. Adv Mater 2019;31:1900647.

[41] Li F, Lu J, Zhang Q, et al. Controlled fabrication, lasing behavior and excitonic recombination dynamics in single crystal $CH_3CH_3PbBr_3$ perovskite cuboids. Sci Bull 2019;64:698–704.

[42] Chen H, Zhou L, Fang Z, et al. Piezoelectric nanogenerator based on *in situ* growth all-inorganic $CsPbBr_3$ perovskite nanocrystals in PVDF fibers with long-term stability. Adv Funct Mater 2021;31:2011073.

[43] Sun J, Hua Q, Zhao M, et al. Stable ultrathin perovskite/polyvinylidene fluoride composite films for imperceptible multi-color fluorescent anti-counterfeiting labels. Adv Mater Technol 2021;6:2100229.

[44] Zhu X, Ge L, Wang Y, et al. Recent advances in enhancing and enriching the optical properties of Cl-based $CsPbX_3$ nanocrystals. Adv Opt Mater 2021;9:2100058.

[45] Xu Z, Jiang X, Cai H-p, et al. Toward a general understanding of exciton self-trapping in metal halide perovskites. J Phys Chem Lett 2021;12:10472–8.

[46] Kim J, Chung C-H, Hong K-H. Understanding of the formation of shallow level defects from the intrinsic defects of lead tri-halide perovskites. Phys Chem Chem Phys 2016;18:27143–7.

[47] Yong Z-Y, Guo S-Q, Ma J-P, et al. Doping-enhanced short-range order of perovskite nanocrystals for near-unity violet luminescence quantum yield. J Am Chem Soc 2018;140:9942–51.

[48] Zhang Z, Kang R, Cheng P, et al. Optical properties of ion accumulation areas in $MAPbX_3$ single crystals. Adv Opt Mater 2021;9:2100850.

[49] Buin A, Comin R, Xu J, et al. Halide-dependent electronic structure of organolead perovskite materials. Chem Mater 2015;27:4405–12.

[50] Mannodi-Kanakkithodi A, Park J-S, Martinson ABF, et al. Defect energetics in pseudo-cubic mixed halide lead perovskites from first-principles. J Phys Chem C 2020;124:16729–38.

[51] Xue H, Brocks G, Tao S. Intrinsic defects in primary halide perovskites: a first-principles study of the thermodynamic trends. Phys Rev Mater 2022;6:055402.

Junlu Sun received his M.S. degree in Materials Science & Engineering and Ph.D. degree in Optics from Zhengzhou University in 2017 and 2021, respectively. He had been a visiting graduate student at Prof. Caofeng Pan's group at Beijing Institute of Nanoenergy and Nanosystems, Chinese Academy of Sciences (CAS). Then he joined the School of Physics and Microelectronics, Zhengzhou University in 2022. His research mainly focuses on flexible stretchable optoelectronics and self-powered display system.

Tianshu Li received her B.S. degree at Jilin University (2016). She is currently a Ph.D. candidate at the School of Materials Science and Engineering, Jilin University under the supervision of Prof. Lijun Zhang. Her research is mainly focused on defect physics in semiconductors, and understanding the fundamental mechanisms of compounds with lone-pair electronic configuration for developing novel optoelectronic materials.

Lin Dong received his B.S. (1998) and M.S. degrees (2001) in Chemistry from Jilin University, and Ph.D. degree (2005) in Condensed Matter Physics from Changchun Institute of Optics, Fine Mechanics and Physics (CIOMP), CAS. He joined Zhengzhou University in 2005. He is currently a professor at School of Physics & Microelectronics, Zhengzhou University. His research interest is mainly focused on mechanoluminescence and piezotronic/piezophototronic derived nanomaterials and devices.

Lijun Zhang is currently a Tang-Aoqing Distinguished professor at the School of Materials Science and Engineering, Jilin University. He obtained his B.S. degree at Northeast Normal University (2003), and Ph.D. degree at Jilin University (2008). He then worked as post-doctoral researcher at Oak Ridge National Laboratory (2008–2010) and National Renewable Energy Laboratory (2010–2013), and became a research assistant professor at University of Colorado at Boulder (2013–2014). His current interest focuses on designing and band structures engineering of functional semiconductor materials for optoelectronic applications.

Chongxin Shan obtained his B.S. degree from Wuhan University in 1999, and Ph.D. degree from CIOMP, CAS in 2004. Then he worked at Chinese University of Hong Kong and University of Nottingham as a postdoctoral researcher, and returned to CIOMP as professor in 2008. He moved to Zhengzhou University in 2015, and has been the Dean of School of Physics & Microelectronics. His research interest is mainly focused on wide band gap semiconductor materials and optoelectronic devices.

Caofeng Pan received his B.S. (2005) and Ph.D. (2010) degrees in Materials Science and Engineering from Tsinghua University. He then joined the group of Prof. Zhong Lin Wang at the Georgia Institute of Technology as a postdoctoral fellow from 2010 to 2013. He is currently a professor and a group leader at the Beijing Institute of Nanoenergy and Nanosystems, CAS. His research interest mainly focuses on piezotronics/piezo phototronics for new electronic and optoelectronic devices, nanopower source, hybrid nanogenerators, and self-powered nanosystems.